Volume 1 | Number 1 | Jan 2013 | Pages 1–100

Journal of
Materials Chemistry B

Materials for biology and medicine
www.rsc.org/materialsB

ROYAL SOCIETY
OF CHEMISTRY

ROYAL SOCIETY
OF CHEMISTRY

www.rsc.org/materialsB

Colloidal nanoparticles of BBT-based narrow-bandgap small molecules as theranostic agents show strong near-infrared photoacoustic signal and high photothermal conversion efficiency.

Journal Name

ARTICLE

A dual-functional benzobisthiadiazole derivative as an effective theranostic agent for near-infrared photoacoustic imaging and photothermal therapy

Shuo Huang,[a] Paul Kumar Upputuri,[a] Hui Liu,[a] Manojit Pramanik,[a,]* Mingfeng Wang [a,]*

Nanoparticles (NPs) with integrated functionalities of targeting, therapy, imaging contrast and biocompatibility have shown promising opportunities for improved disease diagnosis and therapy. Here, we report a theranostic agent based on a narrow-bandgap small molecule, benzo[1,2-c;4,5-c']bis[1,2,5]thiadiazole-4,7-bis(9,9-dioctyl-9H-fluoren-2-yl)thiophene (denoted as BBT-2FT), with strong absorption of near infrared (NIR) light. Colloidal nanoparticles composed of BBT-2FT show photoacoustic signal intensity 10 times higher than that of blood, and high photothermal conversion efficiency (η = 40%) under irradiation of 808-nm laser light that kills over 90% HeLa cells in 10 mins.

Introduction

Theranostic, defined as a material that combines the modalities of therapy and diagnosis, has attracted great attention since it was coined in 2002[1-3]. Before starting treatments to various diseases such as cancer, it is important to monitor and understand the status and locations of the disease. In contrast to using two separate agents, theranostic aims to incorporate various agents into one material, in order to realize imaging and therapy simultaneously. For instance, some of the therapeutic strategies developed for different types of cancer treatments, such as nucleic therapy, chemotherapy, photothermal therapy, photodynamic therapy, and radiation therapy, can be integrated with imaging techniques, such as magnetic resonance imaging (MRI), nuclear imaging (PET/CT), photoacoustic imaging, and fluorescence imaging [4-10].

Among a variety of diagnosis techniques, photoacoustic tomography (PAT) is a promising medical imaging technique that combines rich optical contrast and scalable high ultrasonic resolution in a single modality[11-14]. PAT can provide deeper tissue imaging than other pure optical imaging modalities (fluorescence microscopy, Raman microscopy, optical coherence tomography, etc.). In PAT, short (nanosecond) non-ionising laser pulses are absorbed by the biological tissue leading to transient thermal expansion of the tissue and subsequent ultrasound emission. The generated ultrasound waves are acquired by ultrasound transducer to form a photoacoustic image. PAT has been proven to be a promising technique for imaging biological features from organelle to organs[14]. The application of PAT includes, but not limited to, small animal brain imaging, breast cancer imaging, monitoring of vascularisation, tumor angiogenesis, blood oxygenation, total haemoglobin concentration, etc. [15-21]

Biological tissues have relatively low absorption in the near infrared (NIR) region[22, 23]. Therefore, NIR light has been used for deep tissue PAT imaging. Several exogenous contrast agents with high absorption in the NIR region have been synthesized and used to enhance the contrast for deep tissue PAT imaging[24]. For example, noble metallic nanoparticles with different shapes such as gold (Au) nanoshells[25], nanorods[26], and nanocages[27, 28], nanobeacons[29, 30] have been widely used as contrast agents for PAT imaging. Other inorganic NPs, such as single-walled carbon nanotubes (SWCNTs)[31, 32] and copper sulphide NPs[33], served as good contrast agents for deep PAT imaging. Quantum dots were also used as multi-modal contrast agent in photoacoustic and photothermal imaging[34]. Nevertheless, the biodegradability and long-term toxicity of these inorganic materials remain an issue for their use in clinical trials. Organic dyes such as indocyanine green (ICG)[35, 36] have better biocompatibility and biodegradability. But they suffer from relatively small optical absorption cross-section, poor photostability, and could be easily removed by the renal system due to their relatively small size (<10 nm). Dye-doped porphysome organic NPs have been reported for PAT imaging[37], but may be limited by their complicated synthesis and relatively large diameter (>100 nm) which could be

[a.] School of Chemical and Biomedical Engineering, Nanyang Technological University, 62 Nanyang Drive, Singapore 637459. E-mail: M. Wang (mfwang@ntu.edu.sg); M. Pramanik (manojit@ntu.edu.sg)

removed by macrophage system mostly by the liver and spleen. Recently, a biocompatible polypyrrole organic NPs (~46 nm in diameter) has been demonstrated for deep tissue imaging in PAT system[38].

Among many strategies for cancer treatment, photothermal therapy has been widely used due to its advantages such as high specificity, minimal invasiveness, low toxicity to normal tissues, and excellent anti-cancer efficacy.[39-41] As a consequence, many efforts have been devoted to explore various theranostic nanomaterials, especially combining NIR photoacoustic imaging and photothermal therapy due to the deep penetration of tissues, high specificity, minimal invasiveness, selective targeting and excellent anti-cancer efficacy. Though many theranostic platforms[42-46] have been established as the combining form of the therapeutic agents and imaging agents, the two agents may slowly dissociate from the carrier at different rates during the circulation in blood, leading to quite different biodistribution and pharmacokinetics. Thus, it is important to explore a photothermal agent, which can serve as a contrast agent itself. To that end, it is necessary to incorporate photoacoustic imaging and photothermal therapy into one agent to realize diagnosis and therapy together. Some dual-modal theranostic materials have been reported, such as combining photoacoustic imaging and PTT using inorganic nanoparticles (NPs)[34, 47-51] and conjugated polymers[52]. However, these inorganic materials still suffer from their poor biocompatibility and biodegradability.

Benzo[1,2-c;4,5-c']bis[1,2,5]thiadiazole (BBT) based derivatives are well-known narrow-bandgap building blocks for organic optoelectronic devices[53-59]. Taking the advantage of the strong light absorption of BBT derivatives in near NIR window that can benefit deep tissue imaging and therapy, Wang and coworkers[60] recently reported that colloidal nanoparticles composed of a small molecular BBT derivative (denoted as BBTEHT) showed high photothermal conversion efficiency and robust photostability compared to gold NPs[61, 62] for effective treatment of cancer cells. We expected that the impressive photothermal performance of BBT derivatives would also enable their applications as contrast agents for photoacoustic imaging, leading to a new type of theranostic agent that integrate the functionality of both photothermal therapy and photoacoustic imaging.

Herein, we report such a theranostic agent based on a small-molecular BBT derivative, benzo[1,2-c;4,5-c']bis[1,2,5]thiadiazole-4,7-bis(9,9-dioctyl-9H-fluoren-2-yl)thiophene (denoted as BBT-2FT). BBT unit, due to its hypervalent sulfur atoms stabilized in quinoidal structures in a conjugated backbone, is a strong electron accepting unit that ensures strong NIR absorption of BBT-2FT in the therapeutic optical window. The biradical nature of BBT unit as well as the presence of thermally accessible triplet states may also contribute to the NIR absorption.[63] The BBT-2FT NPs prepared through nanoprecipitation in the presence of block polymer PEG-*b*-PCL possess excellent stability and biocompatiblity in the absence of NIR light irradiation. The NPs not only demonstrated high photothermal conversion efficiency under

808 nm laser irradiation that killed over 90% HeLa cells in 10 min, but also served as a good photoacoustic imaging contrast agent and provided strong photoacoustic signal compared to blood for bioimaging purpose.

Results and discussion
The preparation and characterization of BBT-2FT NPs
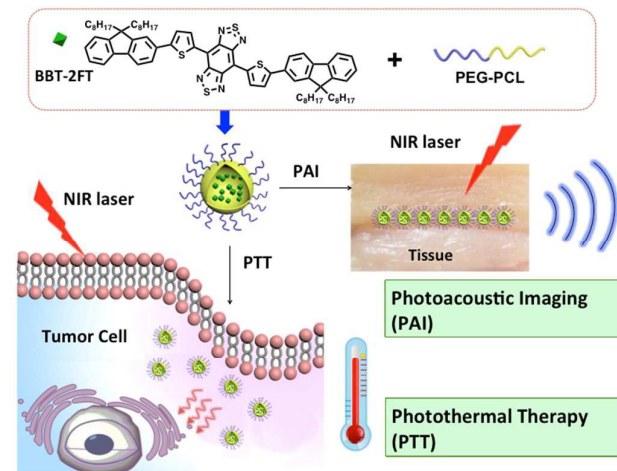
Scheme 1. Schematic illustration of the preparation of BBT-2FT nanoparticles and their applications in NIR photothermal therapy and photoacoustic imaging.

Scheme 1 shows the molecular structure of BBT-2FT and a schematic presentation of the NPs formed through a nanoprecipitation process. Narrow-band gap molecule BBT-2FT was synthesized following a procedure described in the SI, which was also confirmed by ^{1}H-NMR (Figure. S2), ^{13}C-NMR, and MALDI-TOF mass spectroscopy (Figure. S1). BBT-2FT showed two absorption peaks in an organic solvent such as THF, one around at 450 nm with small shoulder and the other at 880 nm, with an onset around 1300 nm. The molar absorption coefficient of BBT-2FT in toluene at 808 nm was calculated to be $2.7 \times 10^4 \ L \cdot Mol^{-1} \cdot cm^{-1}$.

In this study, we chose an amphiphilic block polymer PEG-*b*-PCL instead of Pluoronic F127 as the stabilizer for the preparation of BBT-2FT colloidal NPs, as some agglomeration of Pluoronic F127 micelles loaded with BBT-EHT was observed under NIR laser light irradiation.[60] Such intermicellar agglomeration can be attributed the relatively low lower critical solution temperature (LCST) of Pluronic F127 compared to that of PEG-*b*-PCL. As a result, Pluronic F127 forms gels in water over a much broader temperature range than PEG-*b*-PCL-*b*-PEG.[64, 65] These results suggest that PEG-*b*-PCL micelles have better photothermal stability than Pluronic F127 micelles, which can benefit their applications in bioiamging and photothermal therapy. PEG-*b*-PCL was synthesized via ring-opening polymerization of β-caprolactone using monomethyl-PEG_{5k} as the initiator. The number average molecular weight (M_n) calculated by GPC was 11000, with the ratio of hydrophylic PEG chain to hydrophobic PCL chain is 1:1, which is consistent with the result calculated by ^{1}H-NMR. Details

about the synthesis and characterization of PEG-*b*-PCL are presented in Supporting Information.

Two methods were tested to prepare the colloidal NPs of BBT-2FT in presence of PEG-*b*-PCL (critical micelle concentration = 5 mg mL^{-1} in water)[66] that not only ensures good biocompatibility, but also enhances colloidal stability of BBT-2FT NPs in water. The experimental details about the preparation of the NPs are described in Supporting Information. Briefly, in Method A, the mixture of BBT-2FT and PEG-*b*-PCL in THF/water (1/10, by volume) was subjected to dialysis against water to remove THF. In Method B, THF in the mixture was removed by evaporation in air under vigorous stirring at room temperature. In both cases, the self-assembly was driven by the hydrophobic interaction between the PCL and BBT-2FT which collapsed to form the core of the NPs, while the hydrophilic PEG forming the shell of the NPs provided colloidal stability.

PEG-*b*-PCL micelles before and after being loaded with BBT-2FT were characterized by both transmission electron microscopy (TEM) and dynamic light scattering (DLS). A representative TEM image of the BBT-2FT-loaded PEG-*b*-PCL micelles prepared by Method A is shown in Figure 1a. Most of the NPs appear spherical with different sizes, while a minor population of tadpole-like particles (labeled by circles in Figure 1a) were also observed. The average diameter of these NPs measured by TEM is 46±11 nm, which is smaller than that (68 nm) measured by DLS in the hydrated state. Both TEM and DLS results showed that the average size of the BBT-2FT-loaded PEG-*b*-PCL micelles was slightly larger than that of PEG-*b*-PCL blank micelles (Figure S7) prepared by the same method. The loading efficiency of BBT-2FT by PEG-*b*-PCL micelles was 93% as calculated using the calibration curve shown in Figure S10. The zeta potential of BBT-2FT NPs in water was -6.41±0.64 mV, indicating the electrically-neutral feature on the surface of NPs from which PEG chains are protruding to the aqueous media. Moreover, these NPs remain colloidally stable and no significant leaching of BBT-2FT was observed in phosphate-buffered saline (PBS) at 37 for at least one week (Figure S11).

Compared to the NPs prepared by Method A, those prepared by Method B appeared more uniform under TEM (Figure S9a-b), although the particle size is generally larger. The BBT-2FT-loaded NPs had an average diameter of 81±13 nm, which is slightly larger than that (76±16 nm) of PEG-*b*-PCL blank micelles. The hydrodynamic diameter of the hydrated micelles in water measured by DLS also increased from 90 to 100 nm after being loaded with BBT-2FT. These micellar particles with suitable sizes are expected to target cancer tissues through enhanced permeation retention (EPR) effect and to prevent a blockage of blood vessels or being eliminated by the body's reticuloendothelial system (RES). Most of the experiments below involved BBT-2FT NPs prepared through Method A unless noted specifically.

BBT-2FT shows a strong NIR absorption peak at 880 nm, which is broader compared to that of commercial ICG molecules (Figure. 1b). The photothermal effect induced by NIR laser illumination at 808 nm with a power density of 1.77 W cm^{-2} for 10 min in the presence of BBT-2FT NPs was

investigated by monitoring the temperature of 1 mL aqueous dispersion of BBT-2FT NPs at various concentrations (25, 50, and 100 μg mL^{-1}). Obvious concentration dependence was observed under laser irradiation of the aqueous dispersions containing BBT-2FT NPs, whereas pure water as a control showed little change in temperature under the same conditions of laser irradiation. We measured the photothermal conversion efficiency following a previously reported method (Supporting information).[67] The η value was calculated to be 47%, which is higher than that of the BBT small molecule that we reported previously[60] and those of other reported photothermal agents such as polypyrrole (η = 40%) and Au nanorods (η = 22%).[67]
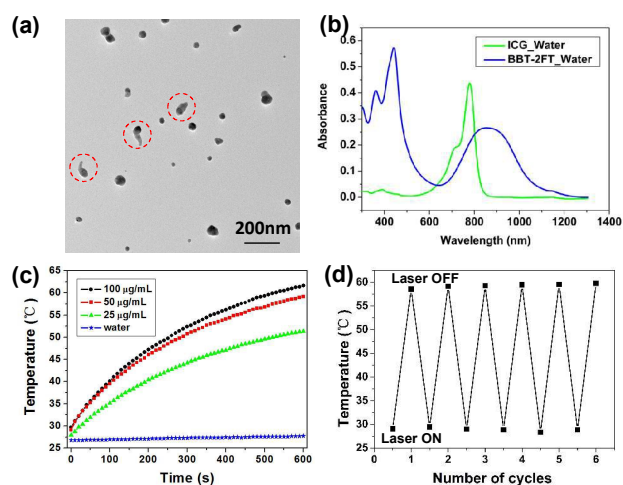

Figure.1 (a) TEM image of BBT-2FT NPs from dispersion of 50 μg mL^{-1}. (b) UV-Vis-NIR spectra of BBT-2FT NPs dispersed in water and ICG water solution. (c) Temperature change plots of different concentrations of BBT-2FT NPs upon irradiation by an 808 nm laser with a power density of 1.77 W/cm^2 for 10 min. (d) Temperature elevation of BBT-2FT NPs over six laser ON/OFF cycles of NIR laser irradiation. All of the NPs presented in this figure were prepared through Method A. All of the concentrations of the BBT-2FT NPs were calculated based on the mass of BBT-2FT without inclusion of the stabilizer.

To further investigate the photostability of BBT-2FT NPs, six cycles of laser ON/OFF with NIR laser were used. The continuous laser (808 nm, 1.77 W/cm^2) instead of high power pulse laser was used to test the photothermal effect, since the pulse laser used in photoacoustic system causes the temperature increasing too fast to record. We note that the continuous laser was also used in the cell experiments described later. Dispersion of BBT-2FT NPs (50 μg mL^{-1}) was irradiated with NIR laser for 10 min (Laser ON, Figure. 1d), followed by naturally cooling (without laser irradiation) to room temperature for 10 min (Laser OFF). This cycle was repeated six times in order to investigate the photostability of BBT-2FT NPs. The recorded temperature change indicated no significant photoinduced degradation of BBT-2FT NPs under the present experimental conditions (Figure 1d). Nevertheless,

the TEM images (Figure S9 c-d) showed some morphological changes of the nanoparticles (prepared via Method B) after laser irradiation. For example, the overall size distribution of the micelles appeared broader (87±19 nm by TEM) after 6 cycles of ON/OFF laser treatment, and some polyhedral nanoparticles were observed. Such changes might be caused by the photothermal annealing effect that induced the local crystallization of the PCL chains within the cores of the micelles. Nevertheless, the morphological and size changes observed under TEM could not be detected by dynamic light scattering (Figure S9 e), suggesting that the average size and colloidal stability of the nanoparticles were not significantly affected by the laser irradiation.

The promising photothermal conversion efficiency of BBT-2FT NPs prompted us to investigate the application of these NPs for photoacoustic imaging as well as photothermal therapy, as discussed below.
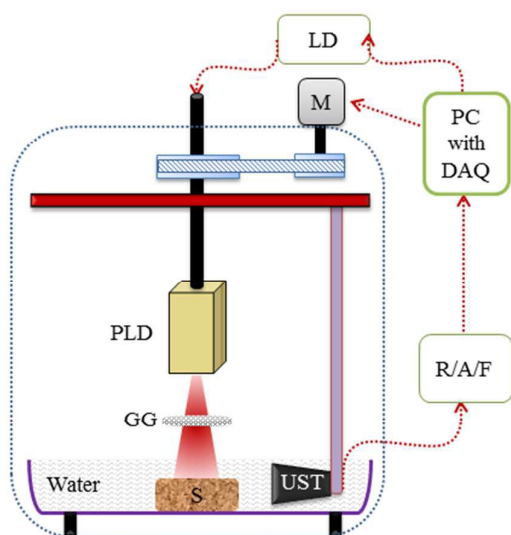

Figure. 2 Schematic diagram of the PLD-PAT imaging system. PLD: Pulsed laser diode, GG: Ground glass, S: Sample, M: Motor, LD: Laser driver, R/A/F: Receiver, amplifier and filter unit, DAQ: Data acquisition card, UST: Ultrasound transducer.

PAT imaging system

The PAT imaging system used in the current study is depicted in Figure. 2. The pulsed laser diode (PLD) (Quantel, France) provides ~136 ns pulses at a wavelength of ~803 nm and pulse energy of ~1.4 mJ at maximum 7 kHz repetition rate. A ground glass (GG) is used to make the laser beam more homogeneous. The sample and the transducer were immersed in water for coupling of PA signal to the ultrasound transducer (UST). The photoacoustic (PA) signal generated by the sample was received by a non-focus transducer (V323-SU/2.25 MHz, Olympus NDT) with 13 mm active area and ~70% nominal bandwidth. The UST was driven by a computer-controlled stepper motor (M) to move continuously in a circular geometry. The signals are subsequently amplified, and band pass filtered by ultrasound signal receiver/amplifier/filter (R/A/F) unit (Olympus-NDT, 5072PR), and then digitized and

recorded by the PC with data acquisition card (DAQ) (GaGe, compuscope 4227) installed in it. Usually, low-frequency ultrasound detectors (1-5 MHz) are used in PAT, so the DAQ card was operated at a sampling frequency of 25 Ms/s. Finally, the computer collected PA signals were used to reconstruct the PA image of the sample using a delay-and-sum back projection reconstruction algorithm.[68]

We note that local temperature rise in the order of few millidegrees can produce photoacoustic signal strong enough for imaging. For instance, one millidegree of temperature rise produces 8 mbar of pressure rise. The ultrasound detectors used for photoacoustic imaging are sensitive enough to record these pressure waves. Moreover, the imaging time is quite short. It has been shown that the photoacoustic cross sectional imaging can be performed as low as in 3 second imaging time.[68] If one uses photoacoustic imaging system based on an ultrasound array transducer, one can obtain photoacoustic imaging in a single laser pulse. Therefore, the photoacoustic imaging itself will not cause any significant temperature rise to initiate the photothermal therapy process.

Photoacoustic signals from blood/BBT-2FT samples

The strong light absorption of BBT-2FT NPs in the NIR region (Figure. 1b) suggests the potential of BBT-2FT as a PAT contrast agent. To compare the PA signal from animal blood and BBT-2FT NPs, we performed experiments on animal blood *vs.* BBT-2FT NPs sample inside a low-density polyethylene (LDPE) tube (inner diameter (ID) = ~0.59 mm, outer diameter (OD) = ~0.78 mm). The PA signal received by the UST was band-pass filtered (1-10 MHz) and amplified with 50 dB gain. Finally, the signal was digitized by a DAQ card at 25 Ms/s and stored in computer. A total of 7,000 A-lines (1 sec) were collected. Figure. 3a shows the PA signals averaged 700 times from animal blood and BBT-2FT NPs (2 mg/mL). One can see that the signal from BBT-2FT NPs is ~10 times stronger than that from blood. Figure. 3b shows that the PA signal intensities increased linearly with the concentration of BBT-2FT NPs.

Deep-tissue imaging experiment

To check the feasibility of BBT-2FT NPs as a PAT contrast agent and determine their effective imaging depth at a wavelength of 803 nm, we acquired PA signals of blood and BBT-2FT NPs embedded inside a chicken breast tissue.

The LDPE tube filled with blood or BBT-2FT NPs (2 mg/mL) was embedded in the chicken breast tissue. PA signals were collected when the tube was placed at 1, 2, 3, or 4 cm deep from the laser illuminated tissue surface. The incident laser energy density on the tissue surface area is ~0.28 mJ/cm^2, which is much less than the "maximum permissible exposure (MPE)" of 32 mJ/cm^2 at 803 nm. Figures. 3c and 3d show the PA signals collected from blood and BBT-2FT (2 mg/mL) at different depths (D) by the 2.25 MHz UST. In our current experiments, blood and BBT-2FT NPs were successfully detected in chicken breast tissue at depth of ~2.0 cm, and ~4.0 cm respectively. The imaging depth can be further increased by using a higher power pulsed laser (for example optical

parametric oscillator (OPO) laser pumped by Nd:YAG laser producing more than 70 times stronger energy per pulse).
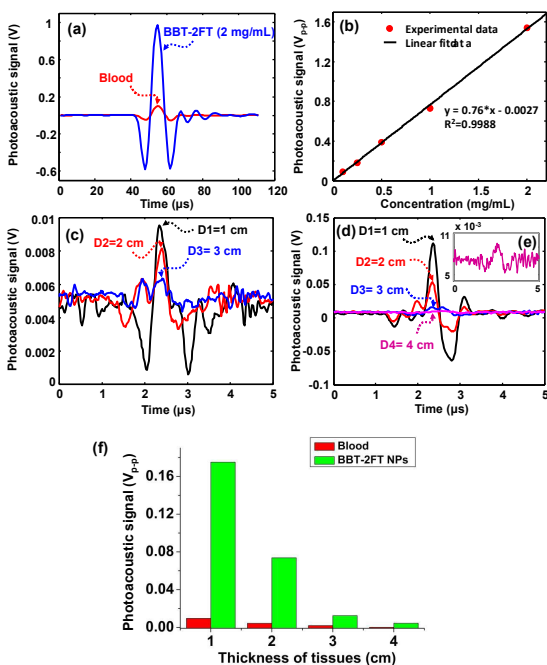

Figure. 3. Photoacoustic (PA) signal of BBT-2FT compared with blood. (a) PA signals of blood and BBT-2FT NPs (2 mg/mL) received by 2.25 MHz UST, (b) PA signal as a function of concentration of BBT-2FT NPs. PA signals generated from blood (c) and BBT-2FT NPs (d) in a LDPE tube embedded inside a chicken breast tissue at difference depths, (e) Zoom in version of the PA signal at D4 = 4 cm. (f) The PA signal of blood and BBT-2FT NPs as a function of penetration depth in chicken tissues.

Deep-tissue imaging experiments were carried out on the sample shown in Figure. 4a, which is made of two LDPE tubes (~ 0.59 mm ID, ~ 0.78 mm OD, ~8 mm long), one filled with blood and other filled with BBT-2FT NPs (2 mg/mL). The two LDPE tubes were placed on a chicken breast tissue as shown in Figure. 4a. For imaging they were covered by tissues of various thicknesses as shown in Figure. 4b. The tissue cross-section containing the LDPE tubes was imaged when tissue slices were sequentially placed to make the tubes 1 cm, and 2 cm deep from laser-illuminated tissue surface. Figure.4c and 4d show the PAT images acquired at 1 cm, and 2 cm depth, respectively. The SNR values of blood, BBT-2FT NPs measured from Figure. 4c are ~23, ~35 and that measured from Figure. 4d are ~9, ~14, respectively. Both the tubes were clearly visible at 2 cm under the chicken breast tissues. Our results indicate that BBT-2FT NPs are promising contrast agents for PAT with good PA signal enhancement and image contrast in biological tissues.

Photothermal therapy *in vitro* experiments
We next investigated the *in vitro* photothermal therapy treatment and cytotoxicity of BBT-2FT NPs. HeLa cells (human cervical carcinoma cell lines) cultured in 12-well plates were

incubated with 25 μg mL^{-1} of BBT-2FT NPs for 6 h, after being rinsed with PBS twice and being resupplied with fresh DMEM culture medium, then the cells were irradiated with an NIR
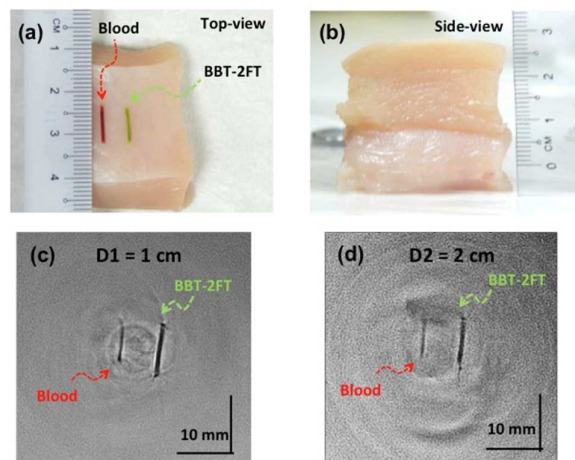

Figure.4. Deep-tissue imaging of blood and BBT-2FT tubes embedded inside chicken breast tissue using PAT system. Photograph of the (a) LDPE tubes with blood and BBT-2FT on chicken tissue, (b) stack of chicken tissue layers inside which the blood and the BBT-2FT tubes were kept. PAT images acquired using 2.25 MHz transducer at 1 cm (c), and 2 cm (d) depth from the light illuminated tissue surface.
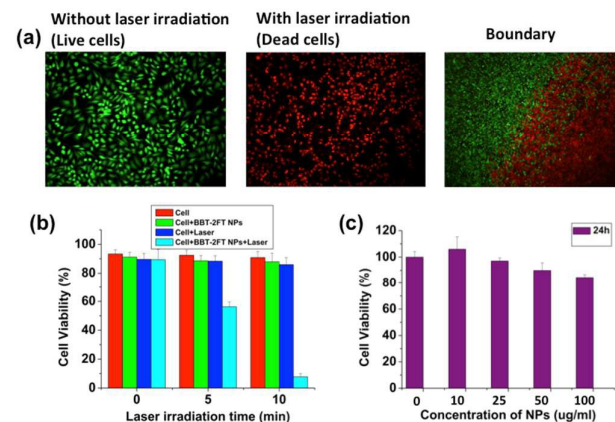

Figure. 5 *In vitro* cell experiments. (a) Fluorescence images of calcein AM/PI co-stained HeLa cells after incubation for 6 h with BBT-2FT NPs (25 μg mL^{-1}) after being irradiated by laser (808 nm and 1.77 W/cm^2) for 10 min. (b) Viabilities of HeLa cells after PTT at different laser irradiation time. Cell viability was normalized to the control group without any treatment. Error bars are based on the standard deviations of five parallel samples. (c) Viability of HeLa cells after being incubated with various concentrations of BBT-2FT NPs for 24 h tested by PrestoBlue® reagent without laser irradiation.

laser (808 nm and 1.77 W/cm^2) for 10 min. Live/dead cells were differentiated by calcein AM (live cells, green fluorescence) and propidium iodide (PI) (dead cells, red fluorescence) co-staining after photothermal therapy

treatment (Figure. 5a). Almost 90% cells were killed after treatments of BBT-2FT NPs and laser irradiation. As shown in Figure. 5a, on the boundary of the laser spot, only cells within the laser spot were killed, showing intense homogeneous red fluorescence. The cells outside the region of the laser spot stayed alive, showing strong green fluorescence.

To evaluate the photothermal cytotoxicity of BBT-2FT NPs in a more quantitative way, HeLa cell lines were irradiated under laser for various time tested by PrestoBlue® reagent. Resazurin ($\lambda_{max.abs}$ = 600 nm) in the PrestoBlue® reagent, a nonfluorescent blue compound, can be reduced in live cells by metabolism to resorufin ($\lambda_{max.abs}$ = 571 nm), which is red in color and highly fluorescent. Since the number of metabolically active cells proportionally correlates with the reduction level, the absorbance readings can be converted and expressed as the percentage reduction of the PrestoBlue® reagent, indicating the relative cell viability. In the experimental group, cells incubated with BBT-2FT NPs for 6 h in a 96-well plate was exposed to the laser for 5 min. At this time point, there was no apparent change in the viability of the three control groups. However, the experimental group at 5 min showed almost 50% dead cells as compared to the control groups (Figure. 5b). When the irradiation time was prolonged to 10 min, there were nearly no viable cells, resulting in close to 100% cell death in the experimental group (Figure. 5b).

To examine the biocompatibility of BBT-2FT NPs, HeLa cells were incubated in NPs dispersions with a series of concentrations for 24 h without laser irradiation. Figure. 5c shows the dose-dependence the cytotoxicity of NPs against HeLa cells. One can see that BBT-2FT NPs show minimal toxicity to HeLa cells without NIR laser irradiation. These results suggest that BBT-2FT NPs can serve as a promising photothermal agent for cancer therapy.

Conclusions

We have presented a dual-modal photoacoustic imaging and photothermal therapeutic agent based on BBT-2FT NPs with strong light absorption in the NIR region. These NPs exhibit good colloidal stability, obviously stronger photoacoustic signal than blood, higher photothermal conversion efficiency, and excellent photostability. Photoacoustic intensity almost 10 times stronger than that of blood was detected, and 4 cm tissue penetration depth makes it viable for *in vivo* applications. Moreover, significant death of HeLa cells was observed due to the hyperthermal effect. These results demonstrate that the BBT–based NPs are promising theranostic agents for cancer imaging and therapy. Further application of these dual functional agents in animals and clinical trial is under investigation, which, if successful, will enable the "see and treat" strategy using a single platform.

Experimental
Materials

All of the chemicals were ordered from Sigma-Aldrich and used without further purification. The synthesis and characterization of BBT-2FT and PEG-*b*-PCL are described in Supporting Information.

General materials characterization:
Transmission electron microscope (TEM) measurements were carried out on a TEM Carl Zeiss Libra 120 Plus operating at an acceleration voltage of 120 kV. UV-vis transmission spectrum was recorded on a Varian Cary 4000 UV-Vis spectrophotometer. ^{1}H NMR spectra and ^{13}C NMR spectra were recorded on a Varian Inova-300 Instrument (300 MHz). MADLI-TOF MS spectra were carried on MALDI TOF/TOF ABI 4800.

General procedure for the synthesis of BBT-2FT colloidal nanoparticles:
Method A: A mixture of 14 mg of BBT-2FT and 83 mg of PEG-PCL was completely dissolved in 1 *mL* of THF overnight. Then 10 *mL* of deionized-water was quickly injected into the mixture under vigorous stirring at room temperature. After being stirred for 5 min, the dispersion was dialyzed against deionized-water by 4 KDa dialysis membranes for 48 h to remove THF. The NPs were separated by centrifugation at 10000 rpm for 5 min and then redispersed in deionized-water before characterization and cell study. The concentrations used for following measurements and cell study are calculated based on the amount of BBT-2FT used in NP preparation.
Method B: A mixture of 14 mg of BBT-2FT and 83 mg of PEG-PCL was completely dissolved in 1 *mL of* THF overnight. Then 10 *mL* of deionized-water was quickly injected into the mixture under vigorous stirring at room temperature. The mixture was continuously stirred for 48 h in a cap-open vial at room temperature to remove THF.

Evaluation of photothermal effect and photostability
The stock dispersion of BBT-2FT NPs was diluted to 100, 50 and 25 µg/mL, respectively. At each concentration, a total of 2 *mL* dispersion was used in the evaluation of its photothermal effect under irradiation of a 808-nm laser with a power density of 1.77 W/cm^{2}. Every sample was irradiated for 10 min and allowed to cool down to the room temperature for the next 10 min, which was counted as one cycle. Water served as the reference group and control group. Temperature was recorded by thermal couple every 10 seconds. To test the stability of sample, we irradiated 2 mL of BBT-2FT NPs dispersion under the 808-nm NIR laser with a power density of 1.77 W/cm^{2} for 6 cycles. Temperature was recorded by thermal couple every 10 seconds.

Calculation of photothermal conversion efficiency
The photothermal conversion efficiency of BBT-2FT NPs was determined according to previous method.[67, 69] The η value was calculated as follow equation:

$$\eta = \frac{hA\,\Delta T_{max} - Q_s}{I \cdot (1 - 10^{-A_\lambda})}$$

where **h** is the heat transfer coefficient, **A** is the surface area of the container, ΔT_{max} is the temperature change of the BBT-2FT solution at the maximum temperature, I is the laser power, A_λ is the absorbance of BBT-2FT at 808 nm, Q_s is the heat change of the solvent, and **η** is the photothermal conversion efficiency. The unknown **hA** value was determined by the linear data of time versus –lnθ curve (Figure S6).

Calculation of BBT-2FT loading efficiency

BBT-2FT NPs prepared via Method A were diluted 100- and 200-fold with THF. The concentration of encapsulated BBT-2FT was calculated using a calibration curve of concentration *vs.* absorbance (830 nm) of BBT-2FT in THF as shown in Figure S10. The loading efficiency was calculated as the percentage of the BBT-2FT remaining in the colloidal NPs *vs.* the original amount of BBT-2FT used in the NP preparation.

Investigation of colloidal stability

The BBT-2FT NPs prepared via Method A were diluted to 50 μg/mL with PBS. 4 mL of diluted BBT-2FT NPs were placed in dialysis membrane ($M_{w,\ cut\ off}$ = 4 KDa) against PBS at 37 °C. The absorbance of BBT-2FT NPs in dialysis membrane was measured to calculate the remaining amount of BBT-2FT.

In vitro experiment

HeLa cells were purchased from American Type Culture Collection (Virginia, USA). HeLa cells were cultured in Dulbecco's Modified Eagle's medium (DMEM) supplemented with 10% (vol/vol) fetal bovine serum (FBS) and 1% penicillin /streptomycin mixture at 37°C with 5% CO_2. Cultures were maintained by adding or replacing the medium every 3-4 days to maintain a cell density of 10^6-10^7 cells per mL. Since HeLa cell lines adhered to the surface of the culture flask during each passaging, the adherent cells were removed by replacing the culture medium by 1× Trypsin (Life Technologies, CA, USA) and putting it back in the incubator for 5 mins. Culture medium was then added to neutralise trypsin and cell counting was performed to check the cell density.

In the photothermal study, a total of 1-mL cell suspension with a cell density of ~1×10^6 cells/mL was transferred to a well plate, where it was mixed with BBT-2FT NPs and incubated for 6 hours in the incubator. After 6 hours, the excess BBT-2FT NPs were washed three times with the culture medium. To evaluate cell death, co-staining dye calcein AM/PI (Sigma-Aldrich, Missouri, USA) was added to the cell sample and was incubated for 15 minutes at 37°C with 5% CO_2, before the observation under a fluorescence microscope. Dead cells were stained by prodium iodide to red fluorescence, and live cells were stained by calcein AM to green fluorescence.

In vitro cytotoxicity

PrestoBlue assay was used to evaluate the effect of different concentrations of BBT-2FT NPs on cell viability in HeLa cells. HeLa cells were seeded on a 96-well plate (10000 cells per well) and cultured at 37 °C with 5% CO_2. After 12 h for attachment, BBT-2FT NPs at four indicated concentrations were added to the medium. After incubation for 24 h, the culture medium was removed and cells were washed three times by 1×PBS to remove excess NPs. Then, PrestoBlue reagent diluted by DMEM were added to each wells and incubated at 37 °C with 5% CO_2. At the same time, PrestoBlue reagents diluted by DMEM were also added to blank wells without cells as control. After 1 h incubation, the absorbance at 571 nm (reference wavelength is 600 nm) was detected by Plate Reader (Tecan Infinite M200 series Pro, Tecan Asia, Singapore). Percentage reduction of PrestoBlue reagent of each sample was calculated according to the formula provided in manufacturer's protocol.

Acknowledgements

Notes and references

1. J. Funkhouser, *Curr. Drug Discovery*, 2002, **2**, 17-19.
2. S. S. Kelkar and T. M. Reineke, *Bioconjug. Chem.*, 2011, **22**, 1879-1903.
3. T. Krasia-Christoforou and T. K. Georgiou, *J. Mater. Chem. B*, 2013, **1**, 3002-3025.
4. A. Ito, M. Shinkai, H. Honda and T. Kobayashi, *J. Biosci. Bioeng.*, 2005, **100**, 1-11.
5. J.-M. Hsieh, M.-L. Ho, P.-W. Wu, P.-T. Chou, T.-T. Tsai and Y. Chi, *Chem. Commun.*, 2006, 615-617.
6. F. L. Primo, M. M. Rodrigues, A. R. Simioni, Z. G. Lacava, P. C. Morais and A. C. Tedesco, *J. Nanosci. Nanotechnol.*, 2008, **8**, 5873-5877.
7. Z. Liu, K. Chen, C. Davis, S. Sherlock, Q. Cao, X. Chen and H. Dai, *Cancer Res.*, 2008, **68**, 6652-6660.
8. J. Yuan, W. Guo, X. Yang and E. Wang, *Anal. Chem.*, 2009, **81**, 362-368.
9. Z. Liu, A. C. Fan, K. Rakhra, S. Sherlock, A. Goodwin, X. Chen, Q. Yang, D. W. Felsher and H. Dai, *Angew. Chem. Int. Ed.*, 2009, **48**, 7668-7672.
10. Y. F. Tan, P. Chandrasekharan, D. Maity, C. X. Yong, K. H. Chuang, Y. Zhao, S. Wang, J. Ding and S. S. Feng, *Biomaterials*, 2011, **32**, 2969-2978.
11. C. Li and L. V. Wang, *Phys. Med. Biol.*, 2009, **54**, R59-97.
12. L. V. Wang, *Nature Photon.*, 2009, **3**, 503-509.
13. P. Beard, *Interface focus*, 2011, **1**, 602-631.
14. L. V. Wang and S. Hu, *Science*, 2012, **335**, 1458-1462.
15. X. Wang, X. Xie, G. Ku, L. V. Wang and G. Stoica, *J. Biomed. Opt.*, 2006, **11**, 024015.
16. L. V. Wang, *Med. Phys.*, 2008, **35**, 5758-5767.
17. E. Z. Zhang, J. G. Laufer, R. B. Pedley and P. C. Beard, *Phys. Med. Biol.*, 2009, **54**, 1035-1046.
18. M. Pramanik and L. V. Wang, *J. Biomed. Opt.*, 2009, **14**, 054024.
19. T. N. Erpelding, C. Kim, M. Pramanik, L. Jankovic, K. Maslov, Z. Guo, J. A. Margenthaler, M. D. Pashley and L. V. Wang, *Radiology*, 2010, **256**, 102-110.
20. S. Hu and L. V. Wang, *J. Biomed. Opt.*, 2010, **15**, 011101.
21. W. F. Xia, D. Piras, M. K. A. Singh, J. C. G. van Hespen, T. G. van Leeuwen, W. Steenbergen and S. Manohar, *Biomed. Opt. Express*, 2013, **4**, 2555-2569.
22. G. Ku and L. V. Wang, *Opt. Lett.*, 2005, **30**, 507-509.
23. L. V. Wang and H.-I. Wu, *Biomedical Optics: Principles and Imaging*, John Wiley & Sons, Inc., New Jersey, 2009.
24. C. Kim, C. Favazza and L. V. Wang, *Chem. Rev.*, 2010, **110**, 2756-2782.
25. Y. Wang, X. Xie, X. Wang, G. Ku, K. L. Gill, D. P. O'Neal, G. Stoica and L. V. Wang, *Nano Lett.*, 2004, **4**, 1689-1692.

26. Y. S. Chen, W. Frey, S. Kim, K. Homan, P. Kruizinga, K. Sokolov and S. Emelianov, *Opt. Express*, 2010, **18**, 8867-8878.

27. X. Yang, S. E. Skrabalak, Z. Y. Li, Y. Xia and L. V. Wang, *Nano Lett.*, 2007, **7**, 3798-3802.

28. K. H. Song, C. Kim, C. M. Cobley, Y. Xia and L. V. Wang, *Nano Lett.*, 2009, **9**, 183-188.

29. D. Pan, M. Pramanik, A. Senpan, S. Ghosh, S. A. Wickline, L. V. Wang and G. M. Lanza, *Biomaterials*, 2010, **31**, 4088-4093.

30. D. Pan, M. Pramanik, S. A. Wickline, L. V. Wang and G. M. Lanza, *Contrast Media Mol. Imaging*, 2011, **6**, 378-388.

31. A. De la Zerda, C. Zavaleta, S. Keren, S. Vaithilingam, S. Bodapati, Z. Liu, J. Levi, B. R. Smith, T. J. Ma, O. Oralkan, Z. Cheng, X. Chen, H. Dai, B. T. Khuri-Yakub and S. S. Gambhir, *Nat. Nanotechnol.*, 2008, **3**, 557-562.

32. M. Pramanik, M. Swierczewska, D. Green, B. Sitharaman and L. V. Wang, *J. Biomed. Opt.*, 2009, **14**, 034018.

33. G. Ku, M. Zhou, S. Song, Q. Huang, J. Hazle and C. Li, *ACS nano*, 2012, **6**, 7489-7496.

34. E. V. Shashkov, M. Everts, E. I. Galanzha and V. P. Zharov, *Nano Lett.*, 2008, **8**, 3953-3958.

35. X. Wang, G. Ku, M. A. Wegiel, D. J. Bornhop, G. Stoica and L. V. Wang, *Opt. Lett.*, 2004, **29**, 730-732.

36. J. Xia, J. Yao and L. V. Wang, *Electromagn Waves (Camb).* 2014, **147**, 1-22.

37. J. F. Lovell, C. S. Jin, E. Huynh, H. Jin, C. Kim, J. L. Rubinstein, W. C. Chan, W. Cao, L. V. Wang and G. Zheng, *Nat. Mater.*, 2011, **10**, 324-332.

38. Z. Zha, Z. Deng, Y. Li, C. Li, J. Wang, S. Wang, E. Qu and Z. Dai, *Nanoscale*, 2013, **5**, 4462-4467.

39. L. Cheng, C. Wang, L. Z. Feng, K. Yang and Z. Liu, *Chem. Rev.*, 2014, **114**, 10869-10939.

40. D. Jaque, L. M. Maestro, B. del Rosal, P. Haro-Gonzalez, A. Benayas, J. L. Plaza, E. M. Rodriguez and J. G. Sole, *Nanoscale*, 2014, **6**, 9494-9530.

41. J. van der Zee, *Ann. Oncol.*, 2002, **13**, 1173-1184.

42. M. Chen, S. Tang, Z. Guo, X. Wang, S. Mo, X. Huang, G. Liu and N. Zheng, *Adv. Mater.*, 2014, **26**, 8210-8216.

43. L. W. Zhang, S. Gao, F. Zhang, K. Yang, Q. J. Ma and L. Zhu, *Acs Nano*, 2014, **8**, 12250-12258.

44. Y. S. Jin, Y. Y. Li, X. B. Ma, Z. B. Zha, L. L. Shi, J. Tian and Z. F. Dai, *Biomaterials*, 2014, **35**, 5795-5804.

45. H. Moon, D. Kumar, H. Kim, C. Sim, J.-H. Chang, J.-M. Kim, H. Kim and D.-K. Lim, *ACS nano*, 2015, **9**, 2711-2719.

46. X. F. Yan, H. Hu, J. Lin, A. J. Jin, G. Niu, S. L. Zhang, P. Huang, B. Z. Shen and X. Y. Chen, *Nanoscale*, 2015, **7**, 2520-2526.

47. J. Shah, S. Park, S. Aglyamov, T. Larson, L. Ma, K. Sokolov, K. Johnston, T. Milner and S. Y. Emelianov, *J. Biomed. Opt.*, 2008, **13**, 034024.

48. P. Huang, J. Lin, W. Li, P. Rong, Z. Wang, S. Wang, X. Wang, X. Sun, M. Aronova, G. Niu, R. D. Leapman, Z. Nie and X. Chen, *Angew. Chem. Int. Ed.* , 2013, **52**, 13958-13964.

49. D. Chen, C. Wang, X. Nie, S. Li, R. Li, M. Guan, Z. Liu, C. Chen, C. Wang, C. Shu and L. Wan, *Adv. Funct. Mater.*. 2014, **24**, 6621-6628.

50. L. Cheng, J. Liu, X. Gu, H. Gong, X. Shi, T. Liu, C. Wang, X. Wang, G. Liu, H. Xing, W. Bu, B. Sun and Z. Liu, *Adv. Mater.*, 2014, **26**, 1886-1893.

51. W. Li, P. Rong, K. Yang, P. Huang, K. Sun and X. Chen, *Biomaterials*, 2015, **45**, 18-26.

52. K. Pu, A. J. Shuhendler, J. V. Jokerst, J. Mei, S. S. Gambhir, Z. Bao and J. Rao, *Nat. Nanotechnol.*, 2014, **9**, 233-239.

53. G. Qian, B. Dai, M. Luo, D. Yu, J. Zhan, Z. Zhang, D. Ma and Z. Y. Wang, *Chem. Mater.*, 2008, **20**, 6208-6216.

54. H. S. Oh, T.-D. Kim, Y.-H. Koh, K.-S. Lee, S. Cho, A. Cartwright and P. N. Prasad, *Chem. Commun.*, 2011, **47**, 8931-8933.

55. J. D. Yuen, J. Fan, J. Seifter, B. Lim, R. Hufschmid, A. J. Heeger and F. Wudl, *J. Am. Chem. Soc.*, 2011, **133**, 20799-20807.

56. J. D. Yuen, R. Kumar, D. Zakhidov, J. Seifter, B. Lim, A. J. Heeger and F. Wudl, *Adv. Mater.*, 2011, **23**, 3780.

57. J. Fan, J. D. Yuen, W. Cui, J. Seifter, A. R. Mohebbi, M. Wang, H. Zhou, A. Heeger and F. Wudl, *Adv. Mater.*, 2012, **24**, 6164-6168.

58. J. Fan, J. D. Yuen, M. Wang, J. Seifter, J.-H. Seo, A. R. Mohebbi, D. Zakhidov, A. Heeger and F. Wudl, *Adv. Mater.*, 2012, **24**, 2186-2190.

59. Y. Wang, T. Kadoya, L. Wang, T. Hayakawa, M. Tokita, T. Mori and T. Michinobu, *J. Mater. Chem. C*, 2015, **3**, 1196-1207.

60. S. Huang, R. K. Kannadorai, Y. Chen, Q. Liu and M. Wang, *Chem. Commun.*, 2015, **51**, 4223-4226.

61. J. Liu, J. Geng, L.-D. Liao, N. Thakor, X. Gao and B. Liu, *Polym. Chem.*, 2014, **5**, 2854-2862.

62. L. Nie, M. Chen, X. Sun, P. Rong, N. Zheng and X. Chen, *Nanoscale*, 2014, **6**, 1271-1276.

63. J. D. Yuen, M. Wang, J. Fan, D. Sheberla, M. Kemei, N. Banerji, M. Scarongella, S. Valouch, T. Pho, R. Kumar, E. C. Chesnut, M. Bendikov and F. Wudl, *J. Polym. Sci. A Polym. Chem.*, 2015, **53**, 287-293.

64. M. Malmsten, *Soft Matter*, 2006, **2**, 760-769.

65. C. Gong, S. Shi, P. Dong, B. Kan, M. Gou, X. Wang, X. Li, F. Luo, X. Zhao, Y. Wei and Z. Qian, *Int. J. Pharm.*, 2009, **365**, 89-99.

66. C. Lu, L. Liu, S.-R. Guo, Y. Zhang, Z. Li and J. Gu, *European Polymer Journal*, 2007, **43**, 1857-1865.

67. Y. Liu, K. Ai, J. Liu, M. Deng, Y. He and L. Lu, *Adv. Mater.*, 2013, **25**, 1353-1359.

68. P. K. Upputuri and M. Pramanik, *Biomed. Opt. Express*, 2015, **6**, 4118-4129.

69. D. K. Roper, W. Ahn and M. Hoepfner, *J. Phys. Chem. C*, 2007, **111**, 3636-3641.